Angular momentum in fission fragments

T. Døssing,[1] S. Åberg,[2] M. Albertsson,[2,3] B. G. Carlsson,[2] and J. Randrup[3]
[1]*Niels Bohr Insitute, University of Copenhagen, DK-2100 Copenhagen Ø, Denmark*
[2]*Mathematical Physics, Lund University, S-221 00 Lund, Sweden*
[3]*Nuclear Science Division, Lawrence Berkeley National Laboratory, Berkeley, California 94720, USA*

(Received 3 July 2023; revised 19 February 2024; accepted 23 February 2024; published 20 March 2024)

We suggest that the angular momentum in fission fragments is generated by statistical excitation at scission. The magnitude of the angular momentum is determined by excitation energy and shell structure in the level density. Treating the prescission shape evolution as a diffusive process, implemented as a Metropolis walk on a five-dimensional potential-energy surface, the average magnitudes of the fission fragment angular momenta are calculated for ^{235}U($n_{\rm th}$, f), assuming that they are perpendicular to the fission axis. The sawtooth behavior of the average angular momentum magnitude as function of mass number is discussed in connection with the similar observed behavior of the average neutron multiplicity, and a good understanding is achieved. The magnitudes of the angular momenta of light and heavy fragments are found to have a weak negative correlation, in accordance with recent experimental results. This correlation arises from the microcanonical sharing of excitation energy by the fragments at scission, where each energy provides a distribution of angular momenta.

DOI: 10.1103/PhysRevC.109.034615

I. INTRODUCTION

A large variety of degrees of freedom may be excited in the fission process, eventually contributing to the excitation energy and the angular momenta of the fission fragments. Energy may be stored as distortion energy, caused by the deviation of the fragment shapes at scission from the equilibrium shapes of the freely moving fragments, which typically carry tens of MeV of intrinsic excitation energy. Furthermore, the fragments are subjected to nuclear and Coulomb potentials at scission and as they move apart.

During the motion of the fully accelerated fragments, after the distortion acquired at scission has been converted to additional internal excitation energy, they undergo decay cascades that have the character of compound nucleus decays. What remains after relaxation of the fission and scission process are the conserved quantities within the fragments, especially the energy and the angular momentum, including both the magnitude and direction of the angular momentum.

Investigations of the decay products from fission fragments give important insight into the fission process. The angular momentum of a fission fragment primarily reveals itself through the γ cascade following neutron evaporation. Early angular correlation experiments [1,2] of ground-band rotational $E2$ transitions show that the angular momentum points preferentially perpendicular to the direction of motion of the fission fragments. Studies of the overall shape of the γ-ray spectrum and the γ-ray multiplicity [3–6] confirm the compound nature of the decay and they also provide a measure of the sum of the two angular momentum magnitudes. The magnitude of the angular momenta of individual fragments can be determined through the side-feeding patterns into low-lying yrast states. In particular, a recent study by Wilson *et al.* [7] yields important information about the angular momentum. The average angular momentum magnitude was found to vary with the fragment mass number A in a sawtooth pattern similar to that displayed by the average neutron multiplicity $\langle\nu\rangle$ [8,9].

Theoretical descriptions of the angular momenta of fission fragments have put different emphasis on the single-particle and collective degrees of freedom. The statistical excitation of nucleons, with dynamical restrictions on the angular momentum coupling, can be framed in terms of the angular momentum carrying modes [10,11]. Conversely, some early studies relate all the excitation energy of the fission fragments to very large deformations of the fragments [12], and a recent study considers most of the angular momentum of the fragments to be generated by this distortion [13]. An early study describes the angular momentum as being generated by vibrations of the nuclei around their tips of contact at scission [14]. A calculation based on time-dependent density functional theory [15] includes both collective and single-particle excitations in generating the angular momentum of fission fragments [16].

A sawtooth behavior of the average angular momentum magnitude versus fragment mass number was obtained in data-based simulation codes [17,18] with certain assumptions on the variation of the moment of inertia with fragment mass number. By projecting angular momentum from Hartree-Fock-Bogoliubov calculated solutions of fission fragments also some kind of sawtooth behavior was obtained in Ref. [19].

We here suggest that the observed strong correlation between the average neutron multiplicity and the average angular momentum magnitude implies that a substantial part of the energy used for neutron evaporation is already available at scission, when the angular momenta of the fission fragments are determined. It follows that the amount of energy stored in fragment distortions at scission (and later on recovered as additional intrinsic energy) plays no role in the determination of angular momenta in the fission fragments.

The dynamics of the nuclear shape is assumed to be strongly damped and the resulting diffusive evolution from the compact equilibrium shape to scission is simulated by Metropolis walks on a potential-energy landscape defined in terms of five shape parameters.

This treatment was introduced in Ref. [20] for calculating fission fragment mass distributions and it has been further developed and applied [21–24]. In those treatments, the statistical weights guiding the random walk were taken as Fermi-gas level densities which are insensitive to the shape of the nuclear system and its specific microscopic structure. By replacing these by microscopic pairing- and shape-dependent level densities [25], it has become possible to not only make more refined studies of mass yields but also to address additional observables in detail, such as the partitioning of the excitation energy between the two fragments [26] and the neutron multiplicities [27]. The present study is concerned with the angular momenta of the fission fragments.

One of the five shape parameters is the neck radius c, the radius of the shrinking connection between the two fledging fragments. The diffusive evolution of the shape, as simulated by the Metropolis walk, is continued until the neck radius has shrunk to a specified critical value, $c_{\rm crit} = 1.5$ fm, at which point it is assumed that scission occurs. While the fragment mass yields and the fragment deformations are not very sensitive to the precise value of $c_{\rm crit}$, the particular value adopted in this study has been found to give the best account of the final kinetic energies of the fragments [26]. At scission, the acquired internal excitation energy is divided between the fragments according to their microscopic level densities with summation over the statistical distribution of the angular momenta in both of the fragments. The microscopic shape-dependent level densities take into account both internal energy and angular momentum of the fragments.

As the originally distorted shape of a fission fragment relaxes towards its equilibrium form, the associated distortion energy is converted to additional internal energy of the fragment. Subsequently neutrons may be emitted, and finally the residual excitation is carried away by a cascade of γ rays. Experiments such as Ref. [7] seek to deduce the fragment angular momenta from the observed γ rays. Model calculations of the angular momentum removed by neutron evaporation have yielded values from less than $1\hbar$ [28] to $(2–3)\hbar$ [17]. The present study assumes that the neutron emission on the average does not change the magnitude of the angular momentum of the fission fragment.

This assumption can be justified within the framework of the Hauser-Feshbach description of statistical decay cascades [29]. After a neutron evaporation, the relative probability of the daughter nucleus having a particular angular momentum I is given by the product of the transmission coefficient and the level density. If the level density decreases as a function of I the nuclear angular momentum will decrease on average, and vice versa if the level density increases with I. For the fragment excitation energies and angular momenta relevant to the present study, shown below in Figs. 2, 5, 8, 10, and 11, the level density is close to a maximum as a function I and there will be no preference for smaller or larger angular momenta in the daughter nucleus after neutron emission. The assumption of little modification of the angular momentum distribution by neutron evaporation is supported by experiments comparing fragment combinations with relatively few and relatively many neutrons evaporated [30,31].

Below, we first discuss, in Sec. II, restrictions on fission fragments angular momenta. Then, in Sec. III, Fermi-gas level densities are provided for two-dimensional angular momentum distributions of fission fragments and a simple analytical relation is obtained between the average angular momentum magnitude and the average neutron multiplicity. Properties of the fledging fragments at scission are discussed in Sec. IV. We apply the calculated results from Ref. [26] of fragments at scission in the reaction ^{235}U$(n_{\rm th}, {\rm f})$. In Sec. V the combinatorial level-density approach, which provides the energy dependence of pairing and shell structure, is used for more accurate calculations of the average angular momentum magnitude for spherical as well as deformed fragments at scission. These results, both the average angular-momentum magnitude versus fragment mass and the correlation between them, are compared with experimental data from Ref. [7] in Sec. VI. In Sec. VII, the results are summarized, and finally in Sec. VIII we discuss the result, the size of angular momentum removed by neutrons, and also some desired experiments.

II. FISSION FRAGMENT ANGULAR MOMENTA

In the present study, the angular momenta of the fission fragments, $\boldsymbol{I}_L$ and $\boldsymbol{I}_H$, are assumed to be perpendicular to the fission axis, and the relevant density of states is then reduced accordingly. For the cases considered here (spontaneous or thermal fission), the magnitude of the angular momentum of the fissioning system is rather small, $I_0 \approx 0$, and the asymptotic direction of the relative fragment motion, is then equal to the fission direction, except for an insignificant Coulomb rotation of 1–2 degrees [28]. Consequently, the fragments emerge with angular momenta that are practically perpendicular to the direction of their relative motion. This feature contrasts with that of an unrestricted scenario in which the fragment angular momenta can point in any direction and where, therefore, the full state density would be relevant.

Figure 1 illustrates how the fragment angular momenta are balanced by the angular momentum of their relative motion, the orbital angular momentum $\boldsymbol{L}$,

$$\boldsymbol{I}_H + \boldsymbol{I}_L + \boldsymbol{L} \approx \boldsymbol{0}, \tag{1}$$

with all the angular-momentum vectors being perpendicular to the fission axis. The rotational modes of a dinuclear system were characterized and named by Nix and Swiatecki [32] and by Moretto [10]. The modes of rotation perpendicular to the fission axis in which the fragment angular momenta are

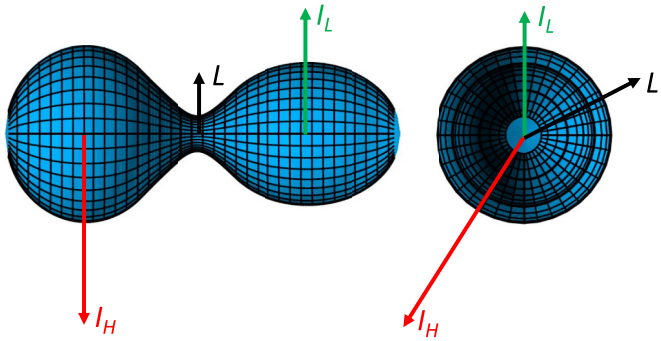

FIG. 1. Illustration of the angular momentum vectors at scission. Both the individual fragment angular momenta, $\boldsymbol{I}_{\rm L}$ and $\boldsymbol{I}_{\rm H}$, and the orbital angular momentum $\boldsymbol{L}$ are perpendicular to the fission axis. The left drawing presents a side view, while the right drawing shows a view along the fission direction.

perpendicular to the dinuclear axis are wriggling and bending, each mode being doubly degenerate because there are two independent perpendicular directions. In wriggling, the two fragments rotate in the same direction and in bending the fragments rotate in opposite directions. A recent discussion of these modes in fission was given in Ref. [11].

Measurements of low-lying $E2$ transitions have shown that the fragment angular momenta are predominantly perpendicular to the direction of fission fragments [1,2]. [Although those experiments were carried out for ^{252}Cf(sf), this feature is expected to hold also for the reaction ^{235}U($n_{\rm th}$, f) considered here.]

Furthermore, recent experiments have shown that the magnitudes of the two fragment angular momenta are at most weakly correlated [7]. This finding shows that *both* wriggling and bending must be populated [18].

III. FERMI-GAS LEVEL DENSITY

Fermi-gas models provide an important background knowledge of level densities and spin distributions. Expressions for a two-dimensional (2D) angular momentum distribution are derived from the Fermi-gas model in Sec. III A. In Sec. III B these expressions are used to obtain a simple analytical expression of the average angular-momentum distribution versus fragment mass number, invoking the experimental data on the average neutron multiplicity to estimate the average excitation energy in the fragments. Important excitation-energy dependent effects from pairing and shell structure are considered in later sections.

A. Fermi-gas distribution of angular momentum

Consider a spherical fission fragment. For a Fermi-gas approximation to the intrinsic fragment excitations, with the condition that the angular momenta be perpendicular to the z axis, $\boldsymbol{I} = (I_x, I_y, 0)$, their distribution is

$$P(I_x, I_y) = \frac{1}{2\pi\sigma^2}\,{\rm e}^{-I^2/2\sigma^2}, \qquad \int P(I_x, I_y)dI_x dI_y = 1. \quad (2)$$

The variance σ^2 (often called the spin cutoff parameter) is given as the product of the temperature and the rigid-body moment of inertia, $\sigma^2 = T\mathcal{J}_{\rm rigid}$. We use standard parameters, $T = \sqrt{E^*/a}$, where E^* is the intrinsic excitation energy and $a = A/(11\ {\rm MeV})$ is the level-density parameter. The rigid-body moment of inertia employed here, $\mathcal{J}_{\rm rigid} = 0.014A^{5/3}\ \hbar^2/{\rm MeV}$, corresponds to a sphere of radius $1.20A^{1/3}$ fm.

In terms of the magnitude I of the angular momentum, the probability distribution (2) corresponds to the spin cutoff level density,

$$\rho_{\rm level}(E^*, I) = \frac{1}{24\sqrt{2}}\frac{2I+1}{\sigma^3}\,{\rm e}^{-I(I+1)/2\sigma^2} \times \frac{1}{(aE^*)^{1/4}}\frac{1}{E^*}\,{\rm e}^{2\sqrt{aE^*}}. \quad (3)$$

For spherical nuclei, the spin cut-off level density is usually discussed in terms of the Bethe subtraction procedure [33]. In experimental measures of the level density, such as for example in thermal neutron resonances, each level of angular momentum I encompasses $(2I+1)$ states with angular momentum projection $M = -I, \ldots, I$. The state density is then obtained by multiplying by this degeneracy,

$$\rho_{\rm state}(E^*, I) = (2I+1)\rho_{\rm level}(E^*, I) \quad (4)$$

corresponding to a 3D angular-momentum distribution, $P(I_x, I_y, I_z)dI_x dI_y dI_z \sim \exp(-I^2/2\sigma^2)dI_x dI_y dI_z$.

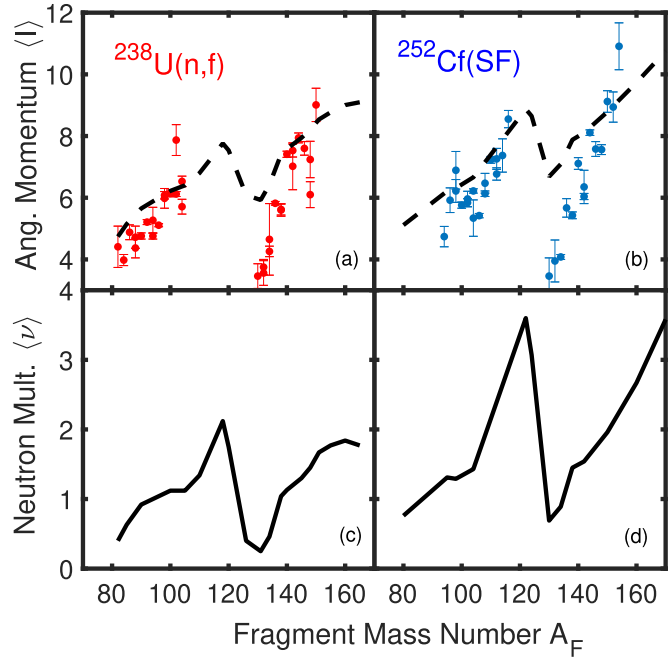

FIG. 2. Estimates of the average angular-momentum magnitude from Eq. (8) (dashed curves in upper parts) calculated at excitation energies derived from estimated/measured average neutron multiplicities (lower parts) for ^{238}U($n_{\rm th}$, f)/^{252}Cf(sf). The experimental data were taken from Ref. [7] for panels (a) and (b), and the estimates for ^{238}U from thermal fission of ^{233}U and ^{235}U from Ref. [34] for (c) and from Ref. [35] for (d).

In Sec. V, where the combinatorial level density is applied, it will be apparent that the spin cutoff estimate (3) with the indicated parameters accounts for the smooth angular-momentum dependence of the level density (see Figs. 4 and 5).

B. Estimates of angular momenta in fission fragments

A recent experimental investigation of several fission cases [7] found that the average angular-momentum magnitude displays a sawtooth pattern as function of the fragment mass number. This behavior is very similar to the observed pattern of the mean neutron multiplicities; see, e.g. [8,9] and Fig. 2. From the average neutron multiplicity $\langle\nu\rangle$, we first make a straightforward estimate of the excitation energy $E^*_{\rm tot}$ of the fragments. Each neutron emission will decrease the excitation energy in the fragment by the separation energy S_n plus the kinetic energy of the neutron, E_n. Neutron evaporation will eventually not be possible when the excitation energy is below the separation energy, which then leaves the fragment with an average energy of about $S_n/2$ to be emitted by γ rays. For a schematic estimate with few parameters,we insert an average separation energy $\langle S_n\rangle = 6$ MeV, kinetic energy $\langle E_n\rangle = 1$ MeV, and energy for γ rays $\langle S_n\rangle/2 = 3$ MeV, yielding the estimate

$$E^*_{\rm tot} = 7\big(\langle\nu\rangle + \tfrac{3}{7}\big)\ \text{MeV}. \tag{5}$$

This is then a measure of the *total* excitation energy of the fully accelerated fragment, $E^*_{\rm tot}$, which is the sum of the intrinsic excitation energy at scission, $E^*_{\rm intr}$, and the energy stored in the shape, the distortion energy $E^*_{\rm dist}$:

$$E^*_{\rm tot} = E^*_{\rm intr} + E^*_{\rm dist}. \tag{6}$$

From the Metropolis random-walk simulations of the shape evolution, it was found that $E^*_{\rm intr}$ accounts for 60–90% of $E^*_{\rm tot}$ [26]. The distortion energy does not contribute to the rotational energy of the fragments since it is recovered only after scission. We schematically account for this effect by applying the average fraction over all mass numbers: $E^*_{\rm intr}/E^*_{\rm tot} = 0.8$.

One more effect should be accounted for, namely the energy of the relative orbital angular momentum of the two fragments at scission. The excitation of the wriggling mode implies the presence of an orbital angular momentum (see Fig. 1), which in the present Fermi-gas approximation also has a Gaussian distribution. This makes it a little more costly in energy to excite the wriggling mode, and the variances of the fragment angular momenta are reduced by the factors f_L and f_H, respectively [18],

$$f_{L,H} = 1 - \frac{\mathcal{J}_{L,H}}{\mathcal{J}_R + \mathcal{J}_L + \mathcal{J}_H}. \tag{7}$$

Generally, the moment of inertia for the relative motion, $\mathcal{J}_R = \mu R^2$ is much larger than those of the individual fragments, $\mathcal{J}_{L,H}$, so the reduction is rather small. Thus $f = \frac{6}{7} \approx 0.86$ for two equal touching spheres.

Using the touching-sphere correction factor and the fact that the average angular momentum for the spin cutoff approximation (3) is $\langle I\rangle = \sqrt{\frac{\pi}{2}}\sigma$, we obtain the following simple expression for the average angular-momentum magnitude in a fission fragment, as a function of the mass number A and the average neutron multiplicity $\langle\nu\rangle$,

$$\langle I\rangle = 0.8^{1/4}\sqrt{\tfrac{6}{7}}\sqrt{\tfrac{\pi}{2}}\sigma = 0.38A^{7/12}\left(\langle\nu\rangle + \frac{3}{7}\right)^{1/4}\hbar, \tag{8}$$

where we have inserted the excitation energy $E^*_{\rm tot} = 7(\langle\nu\rangle + \frac{3}{7})$ MeV for each mass number, together with the standard level-density parameters mentioned above. This simple equation relates the average neutron multiplicity to the average angular-momentum magnitude, which are both properties that can be obtained from experimental data.

The rough estimate (8) is compared to data in Fig. 2. Since neutron multiplicity data do not exist for ^{238}U, we show result from an extrapolation of measured data from ^{233}U and ^{235}U, as suggested in [34]. As can be seen, this simple calculation yields an overall good agreement with the experimental results. While $\langle\nu\rangle + \frac{3}{7}$ varies by about a factor of four between minima and maxima, $\langle I\rangle$ varies only within a factor of 1.5 due to the quarter power in Eq. (8), $\langle I\rangle \propto (\langle\nu\rangle + \frac{3}{7})^{1/4}\hbar$.

Equation (8) was obtained from simple approximations. A more precise result is obtained in Sec. V using the average angular-momentum magnitudes obtained from detailed calculations with the combinatorial level density for realistic scission shapes generated by Metropolis simulations of the shape evolution.

IV. PROPERTIES AT SCISSION

We consider the neutron-induced fission reaction ^{235}U$(n_{\rm th}, {\rm f})$ studied in [26]. In that work, the diffusive shape evolution was followed by means of random walks until the neck radius has fallen below the specified critical value, $c_{\rm crit} = 1.5$ fm, where scission is assumed to occur. The masses (A_L and A_H) and shapes (ε_L and ε_H) of the two fragments are then extracted, together with the total intrinsic excitation energy, $E^*_{\rm intr}$, and the CM distance between the fragments, $R_{\rm sciss}$. The partitioning of $E^*_{\rm intr}$ between the two fragments is governed by the shape-dependent combinatorial level densities of the distorted fragments as described in Ref. [26],

$$P(E^*_L, E^*_H) \ \propto\ \rho(E^*_L, \varepsilon_L)\,\rho(E^*_H, \varepsilon_H), \tag{9}$$

with $E^*_H + E^*_L = E^*_{\rm intr}$.

The present study focuses on even-even fission fragments, selecting 15 even-even nuclei with Z/A ratios close to that of ^{236}U. This covers the mass range from $A = 82$ to $A = 154$ and includes all even charge numbers from $Z = 32$ to $Z = 60$. Their properties are listed in Table I. It may be noted that the quadrupole deformations of the fragments at scission are generally rather small, typically smaller than the ground-state values. Such rather compact scission shapes were also found in early macroscopic calculations of strongly damped fission dynamics [36] as well as in modern Langevin treatments [37]. The fairly small differences between scission shapes and ground-state shapes result in relatively small distortion energies, as discussed above.

Figure 3 displays the energies at scission. The average total excitation energy, solid blue curve in panel (a), is determined by the Metropolis walks, governed by the level density of the

TABLE I. The even-even nuclei included in the present calculation as fragments from the reaction ^{235}U($n_{\rm th}$, f), with the symmetric split shown in bold. For each fragment is shown its ground-state shape [38] and the average values of its end-cap deformation at scission, its intrinsic excitation energy [26] at scission, and the CM distance between the fragment partners at scission. (The ground state shapes for ^{144}56 and ^{148}58 also have octupole deformations, $\epsilon_3 = 0.09$ and 0.07.) The last column indicates which form of the level density to apply at scission, spherical (sph) or deformed (def), see Sec. V C.

		Ground-state shape			Scission shape	$E^*_{L/H}$ at scission	CM dist. at sciss.	sph or
A	Z	ϵ_2	ϵ_4	ϵ_6	ε	(MeV)	(fm)	def
82	32	0.02	0.00	0.00	0.07	3.9	18.8	sph
88	34	0.16	0.02	0.00	0.10	5.7	18.5	sph
92	36	0.22	0.04	0.00	0.14	6.9	18.0	sph
98	38	0.32	0.00	0.00	0.19	10.0	17.5	def
102	40	0.34	0.02	0.01	0.24	11.4	17.1	def
108	42	0.30	0.05	−0.01	0.28	10.6	16.9	def
112	44	−0.25	0.07	0.00	0.32	8.9	17.1	def
118	**46**	−0.22	0.07	0.01	0.13	8.4	18.5	sph
124	48	0.00	0.00	0.00	−0.10	8.4	17.1	sph
128	50	0.00	0.00	0.00	−0.10	8.4	16.9	sph
134	52	0.00	0.00	0.00	−0.08	9.3	17.1	sph
138	54	0.00	0.00	0.00	−0.06	10.1	17.5	sph
144	56	0.15	−0.05	0.02	−0.03	11.6	18.0	sph
148	58	0.19	−0.05	0.02	0.02	12.2	18.5	sph
154	60	0.25	−0.06	0.03	0.07	13.1	18.8	sph

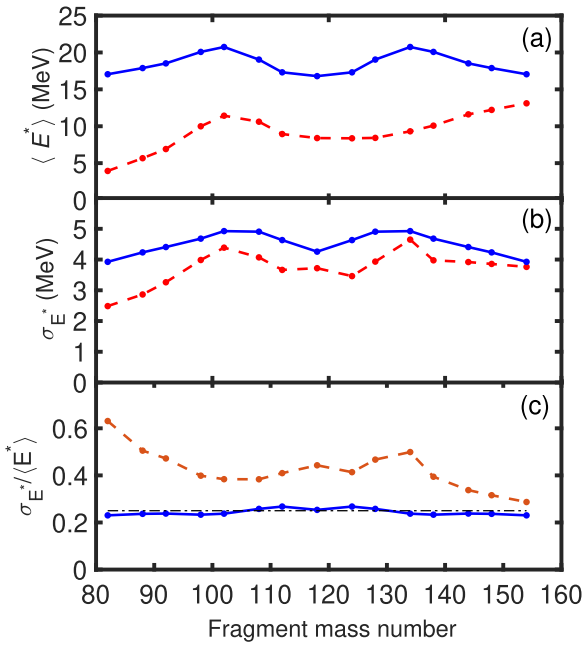

FIG. 3. Intrinsic excitation energy at scission versus fragment mass number: (a) the average intrinsic energy, $\langle E^*_{\rm intr}\rangle$, (b) the associated dispersion, σ_{E^*}, and (c) the relative dispersion, $\sigma_{E*}/\langle E^*_{\rm intr}\rangle$. The values for each fragment are indicated by red dots connected by dashed lines, while the values for the combined system are shown by blue dots connected by solid lines. The black dot-dashed line in (c) shows the constant value 0.25.

overall shape of the ^{236}U nucleus. The diffusion along the asymmetric valley depends smoothly on the mass asymmetry coordinate [25], without any specific signs of the mass 132 closed shells. This results in a smooth dependence of the total excitation energy as function of the fragment mass. The specific low level density at mass numbers around 132 subsequently reveals itself in the distribution of excitation energy on the fragments, as discussed and illustrated in Ref. [27]. The shell structure manifests itself significantly in the excitation energies of the fragments, displayed by the dashes red curves on Fig. 3. To quote some numbers, for masses $A = 128$ and 134 compared to their partners, $A = 108$ and 102, the ratio between average excitation energies is $\langle E^*_H\rangle/\langle E^*_L\rangle \approx 0.8$, to be compared to the Fermi-gas value 1.25.

Due to the diffusive nature of the nuclear shape evolution, the quantities extracted at scission fluctuate from one event to another, and the corresponding distributions may be characterized by their mean values and the associated dispersions. The fluctuations of the fragment excitation energies are quite substantial, as shown in Fig. 3(b). Furthermore, the mass dependence of the dispersion of the combined excitation energy is very similar to that of the mean excitation, so the ratio is approximately independent of mass number, $\sigma_{E^*}/\langle E^*_{\rm intr}\rangle \approx 0.25$, as seen in Fig. 3(c), while the relative fluctuations of the individual excitation energies, $\sigma_{L/H}/\langle E^*_{L/H}\rangle$, are larger and exhibit an overall decrease with mass number.

V. COMBINATORIAL LEVEL DENSITY AT SCISSION

The fission-fragment mass distribution is sensitive to both shell structure and pairing correlations and those should also be included in the calculation of the angular momenta of the fission fragments. This is done by employing the combinatorial level density developed in Ref. [39]. It has mainly been applied to the deformed rare-earth region where it has accounted for the overall level density at energies up to the neutron separation energy [39] and for the angular-momentum dependent odd-even staggering in the number of levels [40]. The present application of the combinatorial level density is based on the folded-Yukawa potential and a monopole pairing interaction. It should be noted that the combinatorial level density is also being used for guiding the diffusive shape evolution that determines the mass distribution and the scission shapes [25], so there is a certain consistency between the treatment of the fission process and the level densities of the emerging fragments.

In Ref. [26] the energy partition at scission was calculated based on Ericsson state densities of the two fragments, while we here use different level densities, as described below. We have checked that while the energy partition is sensitive to the overall shell structure, it is not sensitive to the exact type of level density employed.

The small deformations of some of the scission shapes (see Table I) pose a special problem because the strong coupling limit of single-particle and collective angular momenta is not valid for such compact shapes.

We calculate angular-momentum distributions at scission and extract average angular-momentum magnitudes for spherical and deformed fragment shapes in Secs. V A and V B,

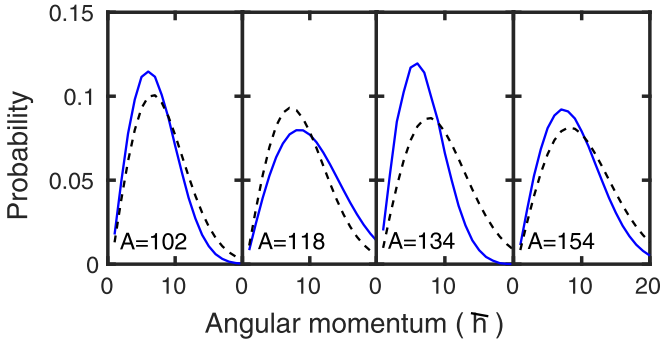

FIG. 4. The distributions of the angular momentum magnitude for four selected fragments with $E^*_{\rm intr} = 10$ MeV. Solid curves: combinatorial level density for a spherical shape; dashed curves: Fermi-gas expression.

respectively. The condition for treating a fragment shape as spherical or deformed is discussed in Sec. V C and the energies and angular momenta of the fragments at scission are then calculated under the two shape conditions in Sec. V D.

The combinatorial level density is calculated for the 15 selected fragments with a bin size in $E^*_{\rm intr}$ of 0.2 MeV up to a maximum of 22 MeV and up to a maximum angular momentum of $38\hbar$.

A. Spherical scission shapes

If the fragments are spherical at scission, the dependence of the level density on the angular momentum I is obtained by the Bethe subtraction procedure [33]. The level density is first evaluated for states of energy E^* and angular-momentum projection M on some axis. The states are degenerate with respect to M, and each projection M encompasses angular momenta from $I = M$ upward, leading to the subtraction relation

$$\rho(E^*, I) = \rho(E^*, M = I) - \rho(E^*, M = I + 1) \qquad (10)$$

With increasing intrinsic energy E^*, the angular-momentum distribution calculated with the combinatorial level density is expected to approach the 2D Fermi-gas expression (3), with the variance given by the product of the temperature and the moment of inertia.

Figure 4 shows the distribution of angular momentum at $E^*_{\rm intr} = 10$ MeV for four different fragment masses, calculated for spherical shapes, together with the spin cut-off approximation with the Fermi-gas parameters (see Sec. II).

The pairing interaction is included in the combinatorial level density, resulting in a backshift, or delay, in the increase of the level density with excitation energy. Pairing then also causes the average angular momentum to be somewhat smaller, so except for $A = 118$ the angular momentum is generally smaller than the Fermi-gas prediction. Particularly small angular-momentum values are found for $A = 134$ where the independent-particle ground state is the $N = 82$ closed neutron shell, combined with $Z = 52$ with only two protons outside the $Z = 50$ closed shell. Conversely, for $A = 118$ the Fermi level is in the middle of partially filled subshells with large single-particle angular momenta, $h\frac{11}{2}$ for neutrons and $g\frac{9}{2}$ for protons.

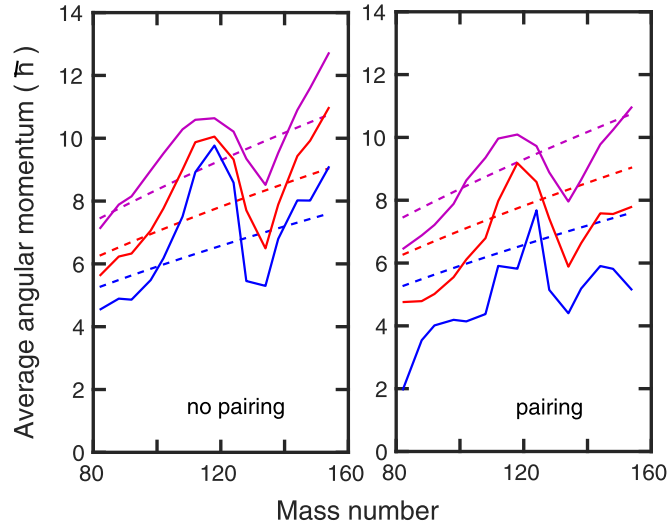

FIG. 5. The mean angular-momentum magnitude for spherical fragments as a function of the mass number A. The left panel shows results obtained without pairing, while the right panel is for pairing included with standard strength. The excitation energies (from below) are $E^*_{\rm intr} = 5$, 10, and 20 MeV. The dashed curves show the corresponding Fermi-gas approximation.

Figure 5 displays the average angular-momentum magnitude, obtained from the angular-momentum distribution for spherical fragments, as a function of mass number for three different excitation energies. For the result without pairing (left panel) substantial shell structure leads to a large variation around the Fermi-gas value $\langle I \rangle = \sqrt{\frac{\pi}{2}}\sigma$, which accounts well for the average behavior with excitation energy and mass number. Pairing generally implies a backshift of the angular-momentum distribution, and consequently lowers the average angular momentum, as seen in the right panel. Lower excitation energy leads to stronger pairing, so the largest effect occurs for $E^*_{\rm intr} = 5$ MeV.

The maxima around $A = 118$ is associated with the partially filled high-j shells, while the minima around $A = 134$ is associated with the shell gaps, as discussed above.

B. Deformed scission shapes

If the fragment shape is clearly deformed, one should apply the level density for deformed nuclei, for angular-momentum coupling in the strong-coupling limit. The assumption of the angular-momentum vector being perpendicular to the fission axis causes important changes of the level density.

The starting point is the many-quasi-particle intrinsic states α of the deformed fragment, having energy e_α and angular-momentum projection K_α. Evaluating the combinatorial level density, each intrinsic state α in combination with its $\mathcal{R}_y(\pi)$-turned partner form the head of a rotational band with a moment of inertia $\mathcal{J}_\alpha$ dependent on the structure of the state α. To obtain the pairing dependence of the moment of inertia, we apply the parametrization discussed in Ref. [41], and the calculated pairing gaps of each configuration yield a specific reduction of the moment of inertia.

This results in the level density of deformed axially symmetric nuclei given by the Ericsson formula,

$$\rho_{\rm Ericsson}(E^*, I) = \frac{1}{2}\sum_{\alpha}\delta\left(E^* - e_\alpha - \frac{I(I+1)-K_\alpha^2}{2\mathcal{J}_\alpha}\right). \quad (11)$$

For simplicity, this expression ignores the special situation for $K = 0$ seniority-zero bands with even angular momentum, which are discussed in detail in Ref. [40].

For small angular momenta I, this level density will be proportional to $2I+1$, caused by the different K values. For example, angular momentum $I = 0$ requires projection $K = 0$, whereas $I = 1$ states have three times as many bandheads, built on $K = -1, 0, 1$. However, for small excitation energies of even-even nuclei, even angular momenta will be more abundant than odd ones, because of the presence of seniority zero rotational bands. With increasing excitation energy, this odd-even effect gradually vanishes, resulting in a smooth angular-momentum distribution [40].

There is a substantial difference between the level density of a deformed fragment at scission and that of an unrestricted deformed nucleus. All shapes of our five-dimensional deformation space are symmetric with respect to a rotation around the fission axis. For a nascent fission fragment, the symmetry axis is then pointing towards the other fragment. But a summation of the level density over the K quantum number for given angular momentum I effectively implies that the deformed shape can point in all possible directions.

The condition that the fragment angular momentum be perpendicular to the symmetry axis restricts the angular-momentum distribution to two dimensions and only $K = 0$ will be possible. However, a rotational band built on top of a $K = 0$ bandhead contains only one state for each value of the angular momentum I, effectively eliminating the factor $2I + 1$ present in the level densities for both spherical and deformed nuclei.

In view of this, we adopt another form of the level density for deformed fission fragments at scission, allowing the angular momentum to acquire a (perpendicular) two-dimensional distribution. That is, only $K = 0$ intrinsic states are included, but the phase space for each angular momentum I is enhanced by the number of directions perpendicular to the fission axis, $2I + 1$:

$$\rho_{\rm sciss}(E^*, I) = \frac{2I+1}{2}\sum_{\alpha, K_\alpha=0}\delta\left(E^* - e_\alpha - \frac{I(I+1)}{2\mathcal{J}_\alpha}\right). \quad (12)$$

With decreasing deformation, the angular-momentum distribution of the scission level density develops smoothly into the two-dimensional Gaussian Fermi-gas distribution (2), provided that the excitation energy is high enough that the pairing correlation is quenched.

C. Conditions for spherical or deformed level density

It is a key question how large the nuclear deformation should be in order for the deformed form of the level density (12) to be appropriate. Usually, the influence of the deformed shape arises in connection with the concept of the rotational enhancement of the level density, caused by the participation of the orientation of the deformed nucleus as an additional degree of freedom. As far as the angular momentum is concerned, there is no rotational enhancement.

The conditions for applying the spherical or the deformed level density depends on the degree of deformation. As discussed by Bjørnholm, Bohr, and Mottelson [42], the rotational collective degree of freedom is generated from a coherent superposition of quasiparticle excitations in the deformed potential, whose energies are typically given by

$$\Delta E \approx \hbar\omega_0|\epsilon_2|, \quad (13)$$

were $\hbar\omega_0$ denotes the intershell distance, and ϵ_2 the deformation. When the average temperature T exceeds this value, the rotational degree of freedom is not independent of the many-quasiparticle excitations making up the level density, and the rotational enhancement should not exist. (It should be mentioned that experimental searches of the fading away of the rotational enhancement with increasing excitation energy have so far not been successful.)

Inserting typical values for the fragments in question, we obtain $|\epsilon_2| > 0.11$ as a quite rough condition for applying the deformed-shape level density. It seems, though, that a somewhat larger deformation is needed for developing the rotational bands, which form the basis of the Ericsson level density as well as the deformed scission level density. This is seen, for example, in the analysis of barium nuclei, from experimental results as well as those calculated with the Monte Carlo shell model [43]. Here, there is a clear change of the low-lying states with increasing neutron number, between ^{142}Ba and ^{144}Ba, with deformations $\epsilon_2 = 0.12$ and $\epsilon_2 = 0.15$, respectively. There is a step towards lower energies of the 2^+ states, as well as towards higher $E(4^+)/E(2^+)$ ratios. The same systematics is seen for other sequences of isotopes or isotones [44] and we take this as a basis for using the fragment end-cap deformation $|\varepsilon| = 0.15$ as the limiting value of the deformation. The resulting scission shape designations are shown in Table I.

D. Excitation energies and angular momenta of fragments

We study below how the distributions of excitation energy and angular momentum of the fission fragments at scission are affected by the use of either spherical- or deformed-shape level densities.

In the simulations of the nuclear shape evolution [26], on which the present study is based, the fragment excitation energies are selected event by event when scission is reached. The level density employed is the Ericsson state density (11), with summation over angular momentum.

We are here more careful about the level density and the angular momentum, while on the other hand we represent the variety of fragment shapes at scission by the average shape for each mass number, or by a sphere for small deformations with $|\varepsilon| < 0.15$. For each shape, we calculate the joint probability for specific excitations and angular momenta,

$$P(E_L^*, I_L, E_H^*, I_H) \sim \rho(E_L^*, I_L)\,\rho(E_H^*, I_H), \quad (14)$$

with the total intrinsic energy $E_{\rm intr}^* = E_L^* + E_H^*$ being sampled from a normal distribution having the mean and dispersion as

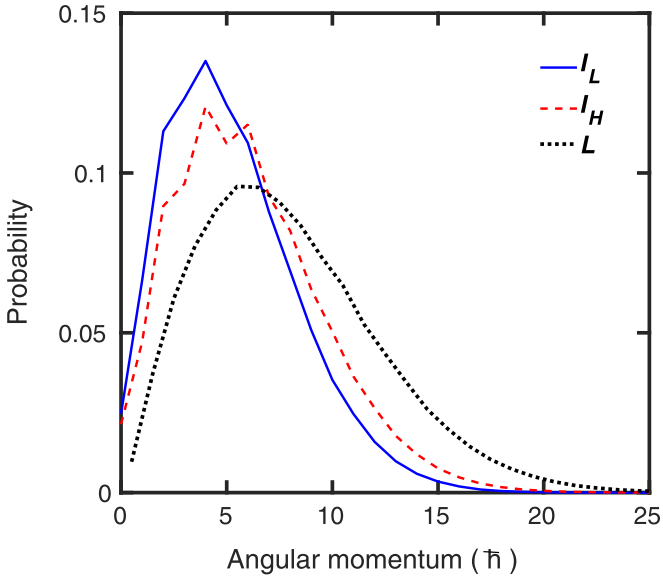

FIG. 6. Angular momentum distributions at scission, $P(I_L)$ and $P(I_H)$ for fragment masses $A_L = 98$ (deformed) and $A_H = 138$ (spherical), and the corresponding distribution of the orbital angular momentum, $P(L)$.

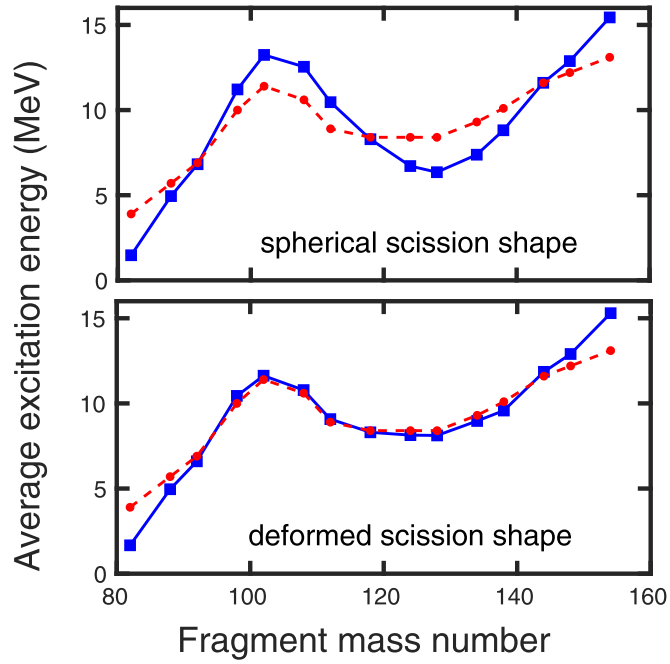

FIG. 7. Calculated average intrinsic excitation energy versus fragment mass number (blue squares connected by solid lines). Level densities are calculated assuming spherical (upper panel) or by deformed (lower panel) scission configurations. Red circles connected dy dashed lines show the excitation energy as calculated by the event-by-event method assuming Ericsson state densities [26].

displayed in Fig. 3. The effect of the wriggling correlation is incorporated by integrating over the relative angle Φ_{LH} between the two angular-momentum vectors in the transverse plane, yielding the orbital angular momentum L (see Fig. 1),

$$L^2 = I_L^2 + I_H^2 + 2I_L I_H \cos\Phi_{LH}. \tag{15}$$

The orbital angular momentum reduces the excitation energy available for exciting the fragments because $E^*_{\rm intr}$ is replaced by $E^*_{\rm intr} - L^2/2\mu R^2$, leading to the following probability distribution for the fragment energies and angular momenta for a specified total intrinsic energy $E^*_{\rm intr}$:

$$\begin{aligned} &P(E^*_L, I_L, E^*_H, I_H)|_{E^*_{\rm intr}} \\ &\quad \propto \int_0^{2\pi} d\Phi_{LH}\, \rho(E^*_L, I_L)\, \rho(E^*_H, I_H) \\ &\quad \times \delta\left(E^*_L + E^*_H - E^*_{\rm intr} + \frac{L(I_L, I_H, \Phi_{LH})^2}{2\mu R^2}\right). \end{aligned} \tag{16}$$

The probability P is subsequently normalized over (E^*_L, E^*_H, I_L, I_H) and an overall probability distribution is obtained subsequently by integrating over $E^*_{\rm intr}$, using a Gaussian distribution with $\langle E^*_{\rm intr}\rangle$ as shown in Fig. 3(a) and a dispersion equal to $\sigma = 0.25\langle E^*_{\rm intr}\rangle$, representing approximately the solid blue curve in Fig. 3(c). (For illustrative purposes, in Sec. VI B we will also calculate for smaller dispersions in $E^*_{\rm intr}$.)

In Fig. 6 the distribution of the magnitude of the orbital angular momentum is shown for the fragments with masses $A_L = 98$ and $A_H = 138$. The coupling of the orbital angular momentum vector to the angular momenta vectors of the light and heavy fragments results in somehat larger average orbital angular momentum magnitude, $\langle L\rangle = 8.0$ as compared to $\langle I_L\rangle = 5.2$ and $\langle I_H\rangle = 6.0$. The typical value of $L = 8\hbar$ gives a small collective rotational energy, $L^2/2\mu R^2$ of the order of 0.1 MeV.

Next, we investigate the average energies in the fragments, comparing the present integral technique with the event-by-event results obtained in Ref. [26].

Figure 7 shows the average intrinsic excitation energies in the fragments, $\langle E^*_{L/H}\rangle$, for different types of shapes and level densities. The top panel shows the results of using spheres for both fragments and correspondingly the Bethe level density for both. One sees that the maxima and minima of the average energy becomes more pronounced for the spherical shape. Generally, the shell structure of nuclear levels is most pronounced for the spherical shape. For the present case, light fragments with mass numbers around 102 to 108 are in mid shell, leading to a large level density, acquiring more excitation energy, being taken from the heavy fragments with mass numbers around 130 to 138, which are close to closed shells.

The lower panel shows the result of using the deformed-shape level density for all fragments. Except for the most light and most heavy fragment, the excitation energy is practically the same as that obtained by the event-by-event sampling. This shows that the average shape is a good representation of the ensemble of shapes encountered event by event. Also, the precise form of the level density does not matter so much here. The Ericsson state density, which was applied in Ref. [26], contains a sum over all rotational bands, with all K quantum numbers, while the deformed-shape level density applied in the present study takes account of only $K = 0$ bands.

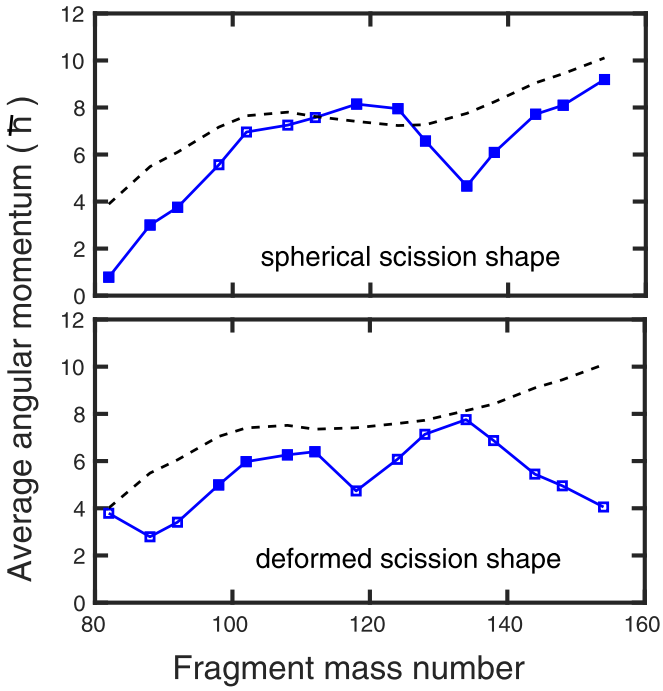

FIG. 8. Calculated average angular momentum versus fragment mass number. Level densities are calculated assuming spherical (upper panel) or deformed (lower panel) scission configurations. Filled squares are used when the deformed/spherical condition applies (see Table I) and open squares are used when it does not apply. Dashed lines show the Fermi-gas result.

Concluding on the average fragment excitation energy, one may say that it is the shell structure of the nucleonic level spectra, and thereby of the nuclear level densities, that determines the partitioning of the energy between the two fragments. To a good approximation the average excitation energy of the light fragment becomes $E_L^* = E_{\rm intr}^* a_L/(a_L + a_H)$, where the level-density parameters a_L and a_H reflect the shell structure at scission. This simplifies to $E_L^* = E_{\rm intr}^* A_L/(A_L + A_H)$ in the Fermi-gas model.

We now turn to the angular momentum obtained by the fragments. In Fig. 8 the calculated average angular momentum as a function of fragment mass number is shown assuming spherical shapes (Sec. V A) for the fragments at scission, and in lower part shows the result of using deformed scission shapes (Sec. V B).

Comparing Figs. 7 and 8, we see that while the fragment excitation energies are very similar when spherical or deformed scission shape level densities are used, the average angular-momentum magnitude is much more sensitive to the type of scission shape assumed. For example, assuming spherical scission shapes implies an increase in angular momentum from mass 134 to 154, while a decrease is found for deformed scission shapes, although the fragment excitation energy increases smoothly in this mass interval (see Fig. 7). The quadrupole deformations of these fledging fragments are indeed very small; see Table I. And since pairing is rather strong and survives up to $E^* \approx 10$ MeV, the moment of inertia $\mathcal{J}$ is strongly reduced to about 10% to 20% of the rigid-body value, according to the employed pairing- and deformation-dependent reduction factor of the moment of inertia [41]. This implies effectively a small spin cutoff parameter, $\sigma^2 = \mathcal{J}T$, and consequently an average angular momentum that may be severely reduced as compared to the nonpaired situation.

E. Significance of closed shells

The variation in average angular momentum with fragment mass obtained for spherical scission shapes (upper panel of Fig. 8) is partly due to single-particle states with different angular-momentum values around the Fermi surface. In the derivation of the Fermi-gas level density, the moment of inertia appears as a product of the density of single-particle states, proportional to the level density parameter a, and the effective square of single-particle angular-momentum projections on a perpendicular axis:

$$\mathcal{J} = \frac{6}{\pi^2}\, a \langle j_x^2 \rangle. \tag{17}$$

For nuclei with proton and neutron numbers around closed shells, there will be gaps in the level spectrum and the above expression serves as guidance, interpreting loosely the quantities a and $\langle j_x^2 \rangle$ as defined locally for the single-particle states close to the Fermi surface. With this interpretation, the appearance of high-j shells around the Fermi surface causes a substantial variation of $\mathcal{J}$ and, consequently, a large variation of the average angular-momentum magnitude.

Strong shell effects of the average angular-momentum magnitude for the spherical shape are seen in Fig. 5. Especially, the upper part of Fig. 8 shows how the sequence of fragments with $A = 124$, 128, and 134 with $Z = 48$, 50, and 52, respectively, acquire quite different average angular momenta, $\langle I \rangle = 8.0\hbar$, $6.2\hbar$, $4.5\hbar$, respectively, although the excitation energies are similar ($E_H^* \approx 7$ MeV).

This behavior can be understood from Fig. 9 showing the average angular-momentum magnitude versus fragment mass for three isotopic chains, calculated for the same average intrinsic excitation energy of 8 MeV. To obtain a realistic distribution of excitation energy in these heavy fragments in the presence of gaps in their level spectrum, we assume that their light partner fragment is spherical and can be described with the Fermi-gas level density (3). The dispersion in the total intrinsic energy is the same as used for the results of Figs. 6 and 7. The average total excitation energy in the calculation is then adjusted to ensure that the average excitation energy in the heavy fragment is $\langle E_H^* \rangle = 8$ MeV.

For each isotopic sequence, there is a maximum in angular momentum for the neutron number $N = 76$, where the Fermi energy is in the middle of the $h\frac{11}{2}$ shell, followed by a distinct minimum at the closed shell at $N = 82$, and then a gradual increase for larger neutron numbers, where the Fermi energy is at the $f\frac{7}{2}$ and $h\frac{9}{2}$ levels. In this way, the values of $\langle I \rangle$ can be interpreted in terms of Eq. (17). The local level density parameter a has a minimum at the shell gap at $N = 82$, and the single-particle angular-momentum projections are on average larger below than above the shell gap. The variation with fragment mass number for the different Z values can be

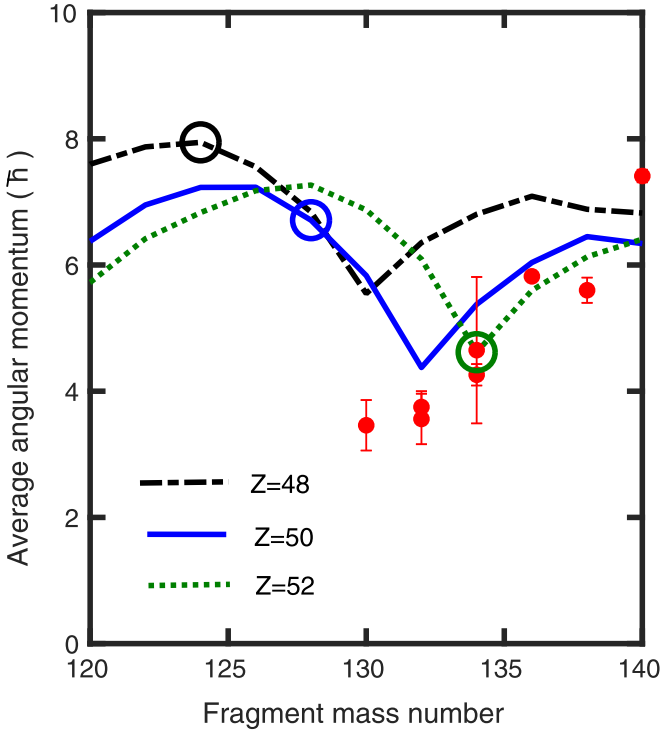

FIG. 9. The average angular momentum magnitude for spherical fragments as a function of mass number for the three isotopic sequences having $Z = 48$, 50, and 52, calculated for the same average intrinsic excitation energy, $\langle E_H^* \rangle = 8$ MeV. The fragments included in the present study (see Table I) are marked by circles. The data from [7] are included (dots with error bars).

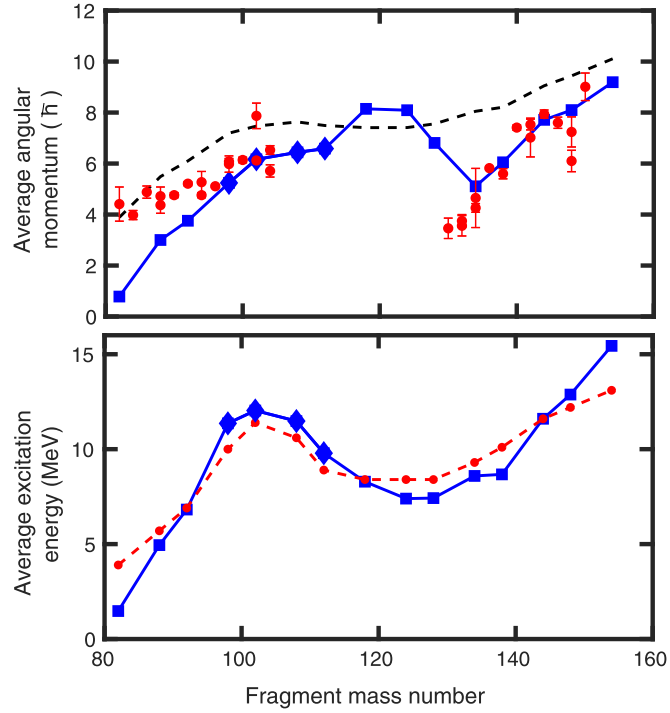

FIG. 10. Upper panel: The average angular momentum magnitude versus the fragment mass number. The data (red dots with error bars) are from Ref. [7]. The calculated values used level densities for either spherical (blue squares) or deformed (blue diamonds) fragments based on the degree of quadrupole deformation at scission (see Table I). The Fermi-gas results are also shown (dashed curve). Lower panel: The corresponding intrinsic fragment excitation energy. Values obtained in Ref. [26] are also shown (red dots connected by the dashed curve).

understood similarly, in particular the minimum of $\langle I \rangle$ at the doubly magic nucleus $^{132}_{82}\mathrm{Sn}_{50}$.

The calculated mass dependence of the average angular momentum for spherical fragments seen in Fig. 8, especially the minimum at $A = 134$, can thus be understood on the basis of this analysis. Certainly, also the excitation energy plays a role in determining $\langle I \rangle$. But the gradual filling of the j shells for spherical fragments explains the main part of the obtained variation in $\langle I \rangle$ as the mass number changes from 112 to 134 while the intrinsic excitation energy exhibits a rather small variation.

The calculations exhibit a trend similar to that of the experimental data (also shown in Fig. 9) which will be discussed below.

VI. COMPARISON TO DATA

Applying the pairing- and shape-dependent combinatorial level density, we now compare our calculations of the fragment angular momenta to data. The calculations are performed for $^{235}\mathrm{U}(n_{\mathrm{th}}, \mathrm{f})$, which we expect to give a result very similar to that for $^{238}\mathrm{U}(n, \mathrm{f})$ for which all data are obtained. In Sec. VI A results of the average angular-momentum magnitude are presented, and in Sec. VI C results of the calculated correlations between the angular momenta of the two fragments are discussed.

A. Average angular-momentum magnitude

Figure 10 shows the final result for the average angular momentum magnitude as a function of fragment mass number, applying the level densities for either spherical or deformed fragments as indicated in Table I. The initial increase of the average magnitude from $A = 80$ up to $A \approx 100$ is caused mainly by the increase in excitation energy, because the Fermi-gas result displays the same behavior. For masses 100 to 154, the Fermi-gas result is rather constant, and the variation of the calculated average angular momentum is caused mainly by the shell structure, most notably the pronounced minimum around $A = 132$ that was discussed in the previous section. This sawtooth behavior corresponds to the sawtooth behavior of the neutron multiplicity [26].

B. Angular momentum with excitation energy from neutron multiplicity

Although the results shown in Fig. 10 are in reasonable overall agreement with the measurements, the calculated average angular-momentum magnitudes around the minimum near $A = 132$ are too large. This deviation is consistent with the overprediction of the local neutron multiplicity, $\langle \nu \rangle \approx 0.6$ [26], whereas the measured values are around $\langle \nu \rangle \approx 0.2$.

To deduce an excitation energy that is consistent with the average neutron multiplicity, one may combine the effect of shell structure in the level density with the excitation energy estimated from measured neutron multiplicities.

To include the shell structure, and to treat the neutron separation energy and kinetic energy consistently, we used the FREYA simulation code [28,45] to generate the distribution of the post-evaporation fragment excitation energy and then calculated the average angular-momentum magnitude for this distribution, which is thus consistent with the average neutron multiplicity. However, due to the simple method of energy sharing used in FREYA, it is generally not possible to be in accordance with the measured neutron multiplicity for both fragments. To remedy this shortcoming, a realistic distribution of excitation energy and angular momentum is generated by representing the complementary fragment by the Fermi-gas level density, as was also done in the calculation of Fig. 8. Because the pre-evaporation intrinsic excitation energies $E^*_{\rm tot}$ include the recovered distortion energies, we obtain the intrinsic excitation energies at scission by the global scaling discussed in Sec. III B, $E^*_{\rm intr} = 0.8\,E^*_{\rm tot}$.

In a display similar to that in Fig. 10, Fig. 11 shows the results obtained with the excitation energies and neutron multiplicities obtained from the FREYA simulations.

The effect of the threshold set by the neutron separation energy is illustrated in the two lower panels of Fig. 10. Between mass numbers 128 and 138, the average neutron multiplicity increases from 0.25 to 1, while the average intrinsic excitation energy only increases from 5.36 to 7.28 MeV.

Altogether, the average angular momenta shown in the top panel of Fig. 10 display a fine agreement between data and calculations, with some reservation for the results around the closed shells near $A \approx 128$. Comparing Figs. 9 and 10 one sees that the adjustment of the excitation energy in accordance with the average neutron separation energy mainly changes the result in two regions: (*i*) the lightest mass number $A = 82$ acquires more energy and thereby more angular momentum, and (*ii*) the nuclei around the closed shell at mass numbers from $A = 124$ to 138 receive about 1.5 MeV less energy, and about $0.8\hbar$ less angular momentum.

Still, the very lowest measured values at mass numbers 130 and 132 are well below the trends of the calculation. One may here refer to Fig. 8, which shows that calculations with different combinations of N and Z may yield lower angular momenta. Such combinations would be in better accordance with the fact that our calculations are for fission of the uranium isotope ^{236}U while the data are for fission of ^{239}U.

Possibly the disagreement at mass numbers 130 and 132 will remain, which might indicate some incomplete excitation of the angular momentum in the dissipation process close to scission for spherical fragments with close-to-magic proton or neutron numbers.

C. Correlation in angular-momentum magnitudes

It is a main result of the paper by Wilson *et al.* [7] that the magnitudes of the angular momenta of the heavy and light fragments are practically uncorrelated, having a slightly negative correlation. Such a negative correlation can be understood within the present treatment of the fission process. Apart from the restriction to the two-dimensional angular-momentum distribution, the entire phase space is being filled in the present study. In some events, the light fragment will acquire an energy that is larger than average and then its angular momentum will typically also be larger than average. In such cases, the opposite will be true for the heavy fragment, which will be colder than the average and its angular momentum will typically be smaller than the average for that given total excitation energy and mass division. Thus, the statistical partitioning of the intrinsic excitation energy by the fragments at scission naturally leads to a negative correlation of the angular momentum magnitudes.

To calculate correlations in angular momenta we sample over energies and angular-momentum vectors as described

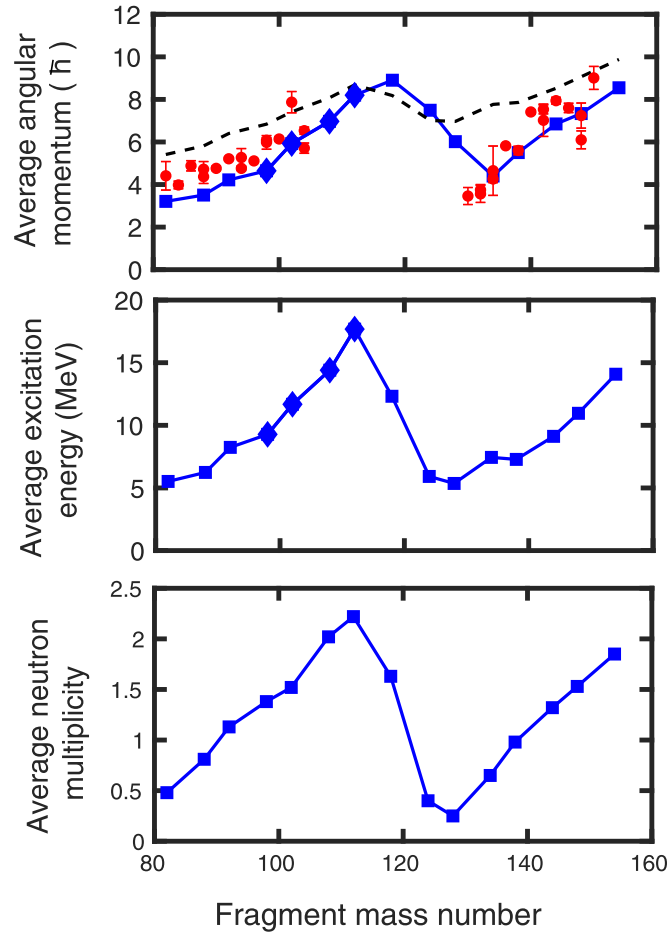

FIG. 11. Upper panel: The average angular momentum magnitudes (blue diamonds) calculated on the basis of the average excitation energies obtained from FREYA simulations and with spherical or deformed fragment shapes as listed in Table I. The Fermi-gas result (dashed curve) and the data from Wilson *et al.* [7] (red dots with error bars) are also shown. Middle panel: The fragment excitation energy determined from the measured neutron multiplicity $\langle\nu\rangle$. Lower panel: The experimental neutron multiplicities (a smooth curve drawn throughout several experimental results as shown in [26]) used as input in the FREYA simulation.

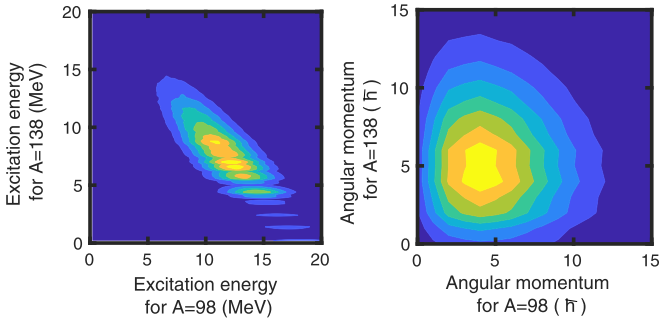

FIG. 12. Contour plot (linear scale) of the probability distributions of excitation energy (left-hand panel) and angular momentum (right-hand panel), for the mass division 98:138. The dispersion in total excitation energy is rather small, 0.1 times the average total energy, resulting in a strong negative correlation of the energies, −0.80. The correlation coefficient between the two angular momenta is −0.059.

in Sec. V D. From the joint probability distribution Eq. (16) one can obtain the correlated probability distribution for the excitation energies E_L^* and E_H^* by summing over the angular momenta I_L and I_H and, similarly, the correlated probability in angular momenta can be obtained by integrating over the energies.

Figures 12 and 13 illustrate the stochastic sampling of excitation energy and angular momentum for the mass numbers A_L:A_H = 98:138. Figure 12 shows the origin of the negative correlation with a schematic calculation, with a small dispersion of the total excitation energy, $\sigma_{\rm intr} = 0.1\langle E^*_{\rm intr}\rangle$. The basic correlation in the energies is apparent, the correlation coefficient being −0.80. For each energy, there is an entire distribution of angular momenta, so the correlation between the excitation energies is significantly diluted for the angular momenta, for which the correlation coefficient is −0.059.

Figure 13 shows the correlations for a realistic dispersion in the total intrinsic excitation energy, namely $\sigma_{\rm intr} = 0.25\langle E^*_{\rm intr}\rangle$ [see Fig. 3(c)]. Here, the energy correlation coefficient is −0.22, while it is only −0.021 for the angular momenta.

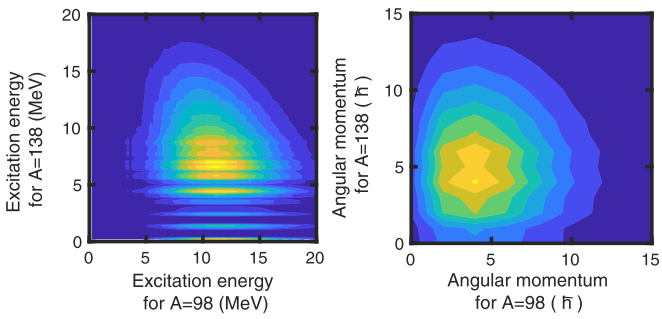

FIG. 13. Same as Fig. 12 but with the dispersion in total excitation energy taken in accordance with experiment, as 0.25 times the average total energy. This results in a negative correlation coefficient between the energies, −0.22, and a weaker correlation coefficient between the angular momenta, −0.021.

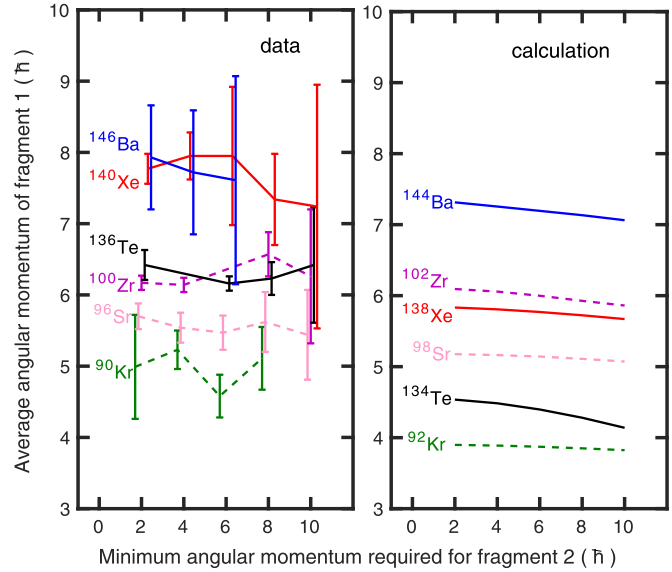

FIG. 14. Correlation in magnitudes of the angular momenta of the two fission fragments, as measured [7] for the fission of ^{239}U in the reaction ^{238}U(n, f) (left-hand side), and as here calculated for the fission of ^{236}U in ^{235}U($n_{\rm th}$, f) (right-hand side).

Figure 14 shows the correlation in angular momenta as obtained by Wilson *et al.* [7] by a gating technique, together with the calculated results of the same observable. Since the data are for final fragments and for the fission of ^{239}U, whereas our calculations are for ^{236}U, the fragments cannot be the same. The gating on the minimum angular momentum of one of the fragments corresponds to horizontal or vertical slices of the joint distribution, such as the one displayed in the right panel of Fig. 13. Clearly, with weak correlations of the magnitudes, this average angular momentum of one fragment will be rather constant, being insensitive to the angular momentum of the other fragment where the cut is made.

It is instructive to display the slopes of a linear fit to the experimental as well as to the calculated curves in Fig. 14, together with the intercept at angular momentum $I = 2$. The result is shown on Fig. 15. For the angular momenta $I = 2$ to 10, the average of the calculated slopes is −0.03, in qualitative accordance with the above discussion of the correlation coefficient. Most of the experimental data display similar slopes, but considering the substantial error bars, together with the positive slope for the fragment ^{100}Zr, the average slope for all data (around −0.015) is not significantly different from zero. The intercept at angular momentum $I = 2$ follows roughly the same trends as seen for the average, displayed in Fig. 10.

A comparison of the results displayed in Figs. 13 and 14 shows a sensitivity to the input value of the dispersion in total intrinsic excitation energy, $\sigma_{\rm intr}$. If $\sigma_{\rm intr}/\langle E^*_{\rm intr}\rangle$ is increased from 0.25 (as obtained in our calculation, see Fig. 3) to 0.3 the correlation coefficients for both the energies and the angular-momenta shift from small negative to small positive values. In this context it should be mentioned that the results displayed in Figs. 9 and 10 for the average angular momentum are rather insensitive to the energy dispersion used in the calculations.

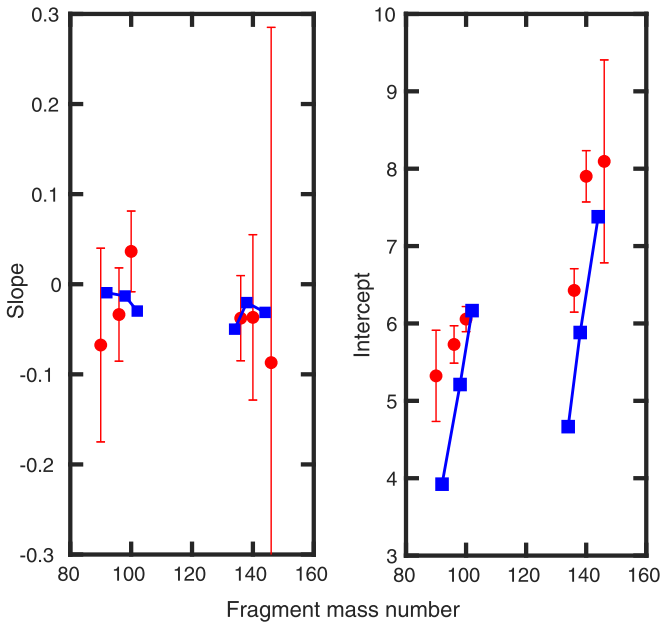

FIG. 15. Slopes (left-hand part) and intercepts at angular momentum $I = 2$ for fragment 2 (right-hand part) obtained from Fig. 14. Experimental values are shown by filled red circles with error bars, and calculated values are shown by filled blue squares.

VII. SUMMARY

The theoretical analysis presented here can describe the recent experimental findings by Wilson *et al.* [7] that the average angular-momentum magnitude displays a sawtooth pattern as a function of the fission fragment mass number and that the angular-momentum magnitudes of the two fragment partners are at most rather weakly correlated.

Our results are partly based on previous simulations of the diffusive shape evolution by means of Metropolis walks on a five-dimensional potential-energy surface, guided by pairing- and shape-dependent combinatorial level densities. This description is based on the idealization of strongly damped shape dynamics from the ground state to scission, controlled by local level densities. When scission is reached, the excitation energy and the angular momentum of each fragment are determined, taking account of the coupling between the individual fragment angular momenta and that of the fragment relative motion. The process produces rather large dispersions in both excitation energies and angular momenta.

The condition that all angular-momentum vectors be perpendicular to the fission axis (Fig. 1) implies a reduced 2D level density, as compared to an unconstrained scenario, and the angular-momentum distributions for spherical or deformed fragments were calculated. Both excitation energy and shell effects in the fragments at scission were found to be important in determining the average angular-momentum magnitude, which was calculated as a function of the fission fragment mass number and compared to recent experimental data. A generally good description was obtained.

For the fragments around the closed shells with $N \approx 82$ and $Z \approx 50$ more comprehensive and illustrative calculations were carried out, showing how the sawtooth minimum in $\langle I \rangle(A)$ arises from the shell structure. Finally, the connection to the average neutron multiplicity was investigated, carrying out calculations with the energy in the fragments determined on the basis of experimental average neutron multiplicities, including the threshold given by the neutron separation energy. This brings the calculated values of the average angular momentum closer to the data, but an overestimation around mass number 128 remains.

Correlations in angular-momentum magnitudes of fission fragments were calculated and found to be in very good agreement with data. The observed very small, and even slightly negative, correlation coefficients were found to appear because of the large dispersion of excitation energies in the two fragments, and the freedom of choosing the two angular-momentum vectors, balanced by the orbital angular-momentum vector. It has been checked that if the kinetic energy associated with the orbital motion is ignored in Eq. (16) (providing complete freedom in the choice of fragment angular momentum vectors), the magnitude of the fragment angular momenta only increases by about 2% for the light fragment, and about 5% for the heavy fragment.

The overall agreement between calculated and measured average angular momenta supports the conjecture that many-particle–many-hole excitations in the fragments are carrying the angular momentum at the point of scission. This provides a statistical distribution of angular momentum with a small dependence on the intrinsic excitation energy [in the Fermi-gas model $\langle I \rangle \propto (E^*_{\rm intr})^{1/4}$]. This simple relation could provide an explanation why angular-momentum magnitude and neutron multiplicity have similar sawtooth behaviors as functions of fragment mass. However, the energy available for neutron emission involves, in addition to the intrinsic excitation energy (defined at scission), also the distortion energy, which is recovered as the shape relaxes from its distorted form at scission to its equilibrium shape during the Coulomb acceleration.

VIII. DISCUSSION

Some important results and assumptions made in the present work are discussed, and desired experiments are suggested. The role of the distortion energy is discussed in Sec. VIII A, and the amount of angular momentum removed by neutrons in Sec. VIII B. Finally, in Sec. VIII C, experiments on the directions of the angular momentum vectors of the fragments are discussed, addressing the assumption of the fragment angular momentum being perpendicular to the fission axis.

A. Role of distortion energy

At scission the excitation energy available in the fissioning nucleus is statistically shared between the two prefragments. Also the angular momentum of each pre-fragment is determined, balanced by the orbital angular momentum. The shapes of the two prefragments are typically different from the ground-state deformations (see Table I) and the associated distortion energy is converted to additional statistical excitation

as the fragment shapes relax to their equilibrium forms. This energy together with the excitation energy from scission is subsequently available for each fragment for the emission of neutrons (and γ rays).

The recovered distortion energy is available for neutron evaporation, while it does not affect the fragment angular momentum, which remains constant after scission. Since it is only the intrinsic excitation energy at scission that determines the angular-momentum distribution, the distortion energy must be relatively small and cannot vary much with fragment mass in order for the same sawtooth behavior to emerge for the angular momentum and the neutron multiplicity. In some early calculations of the neutron multiplicity [12], and also in more recent HFB calculations with the Gogny interaction [46], all energy available for neutron emission was calculated as distortion energy, thus making it hard to explain the observed similar sawtooth behaviors of $\langle I\rangle(A)$ and $\langle\nu\rangle(A)$. From the Metropolis simulations of the shape evolution, the distortion energy was found to be relatively small and smoothly varying with mass number, amounting to 10–30% of the total fragment energy. In general, this finding supports the assumption of strongly damped shape dynamics during fission.

In principle, the question of the amount of the total excitation energy of the fission fragment at different stages of the fission process or the importance and size of the distortion energy might be clarified by measuring correlations between $\nu(A_\mathrm{f})$ and $I(A_\mathrm{f})$ and their variation with fragment mass number.

B. Angular momentum carried by neutrons

When comparing the calculated average angular momentum magnitude with data we assume that the evaporation of neutrons and the statistical $E1$ γ cascade removes only a small amount of angular momentum, less than one unit of $\hbar$. Concerning the angular momentum removed by neutrons, Ref. [17] interestingly points out the occurrence of p and f strength in the neutron evaporation from the fission fragments. In the calculations of the neutron evaporation in Ref. [17], the level density has the spin cutoff form given in Eq. (3), with the moment of inertia chosen as half the rigid-body moment of inertia [47]. And it is found that each evaporated neutron removes about $1.33\hbar$ of angular momentum from the exited fragment [17].

With the high angular momentum to start out with according to Ref. [17], of the order of $8\hbar$ to $10\hbar$, and the rather small moment of inertia, it is indeed favorable to end up at smaller angular momenta by neutron evaporation according to Hauser-Feshbach statistical decay calculations. Comparing level densities at neighboring angular momenta, one finds a ratio of level densities $\rho(I=8)/\rho(I=9)\approx 1.9$ for excitation energy 4 MeV, relevant for the daughter nucleus level density. For our calculations, the average angular momentum is around $6\hbar$ to $7\hbar$, and this yields the level-density ratio $\rho(I=6)/\rho(I=7)\approx 1.25$ at 4 MeV for the combinatorial level density, obtained as an average over all masses. The drive towards smaller angular momenta in the neutron evaporation will then be rather small, even with appreciable $f_{7/2}$ strength in the wave function of the evaporated neutron.

The amount of angular momentum carried by neutrons can be investigated in experiments on the distribution of neutron velocities relative to the motion of the fragments.

C. Direction of fragment angular momenta

A basic assumption in this paper is that the angular momenta of the fission fragments are directed perpendicular to the direction of motion of the fission fragments. This assumption is based on almost 50 year old experiments [1,2], measuring the angular distribution relative to the fission axis of rotational $E2$ transitions along low-lying rotational bands of fragments from the spontaneous fission of ^{252}Cf. Certainly, it would be of great value if such angular distributions could be investigated for neutron induced fission. It would also be of great interest to address (in detail) the angular distribution of the statistical $E1$ transitions which yield information on the angular momentum removed by statistical γ rays. Also, if such experiments could be carried out at above-thermal energies, it could give further information on the shape diffusion process.

ACKNOWLEDGMENTS

We thank Jon Wilson and Peter Möller for illuminating discussions. M.A. was supported by the Swedish Research Council under Grant No. 2022-00223.

[1] J. B. Wilhelmy, E. Cheifetz, R. C. Jared, S. G. Thompson, H. R. Bowman, and J. O. Rasmussun, Phys. Rev. C **5**, 2041 (1972).
[2] A. Wolf and E. Cheifetz, Phys. Rev. C **13**, 1952 (1976).
[3] A. Oberstedt, R. Billnert, A. Gatera, A. Göök, and S. Oberstedt, EPJ Web Conf. **169**, 00014 (2018).
[4] L. Qi, M. Lebois, J. N. Wilson, A. Chatillon, S. Courtin, G. Fruet, G. Georgiev, D. G. Jenkins, B. Laurent, L. LeMeur, A. Maj, P. Marini, I. Matea, L. Morris, V. Nanal, P. Napiorkowski, A. Oberstedt, S. Oberstedt, C. Schmitt, O. Serot *et al.*, Phys. Rev. C **98**, 014612 (2018).
[5] A. Chyzh *et al.*, Phys. Lett. B **782**, 652 (2018)
[6] D. Gjestvang, S. Siem, F. Zeiser, J. Randrup, R. Vogt, J. N. Wilson, F. Bello-Garrote, L. A. Bernstein, D. L. Bleuel, M. Guttormsen, A. Gorgen, A. C. Larsen, K. L. Malatji, E. F. Matthews, A. Oberstedt, S. Oberstedt, T. Tornyi, G. M. Tveten, and A. S. Voyles, Phys. Rev. C **103**, 034609 (2021).
[7] J. N. Wilson, D. Thisse, M. Lebois, N. Jovancevic, D. Gjestvang *et al.*, Nature (London) **590**, 566 (2021).
[8] K. Nishio, Y. Nakagome, H. Yamamoto, and I. Kimura, Nucl. Phys. A **632**, 540 (1998).
[9] A. S. Vorobyev. O. A. Shcherbakov, A. M. Gagarski, G. V. Val'ski, and G. A. Petrov, EPJ Web Conf. **8**, 03004 (2010).
[10] L. G. Moretto and R. P. Schmitt, Phys. Rev. C **21**, 204 (1980).
[11] J. Randrup, T. Døssing, and R. Vogt, Phys. Rev. C **106**, 014609 (2022).

[12] B. D. Wilkins, E. P. Steinberg, and R. R. Chasman, Phys. Rev. C **14**, 1832 (1976).
[13] G. F. Bertsch, T. Kawano, and L. M. Robledo, Phys. Rev. C **99**, 034603 (2019).
[14] J. O. Rasmussen, W. Nörenberg, and H. J. Mang, Nucl. Phys. A **136**, 465 (1969).
[15] A. Bulgac, S. Jin, K. J. Roche, N. Schunck, and I. Stetcu, Phys. Rev. C **100**, 034615 (2019).
[16] A. Bulgac, I. Abdurrahman, K. Godbey, and I. Stetcu, Phys. Rev. Lett. **128**, 022501 (2022).
[17] I. Stetcu, A. E. Lovell, P. Talou, T. Kawano, S. Marin, S. A. Pozzi, and A. Bulgac, Phys. Rev. Lett. **127**, 222502 (2021).
[18] J. Randrup and R. Vogt, Phys. Rev. Lett. **127**, 062502 (2021).
[19] P. Marević, N. Schunck, J. Randrup, and R. Vogt, Phys. Rev. C **104**, L021601 (2021).
[20] J. Randrup and P. Möller, Phys. Rev. Lett. **106**, 132503 (2011).
[21] J. Randrup, P. Möller, and A. J. Sierk, Phys. Rev. C **84**, 034613 (2011).
[22] P. Möller, J. Randrup, and A. J. Sierk, Phys. Rev. C **85**, 024306 (2012).
[23] J. Randrup and P. Möller, Phys. Rev. C **88**, 064606 (2013).
[24] P. Möller and J. Randrup, Phys. Rev. C **91**, 044316 (2015).
[25] D. E. Ward, B. G. Carlsson, T. Døssing, P. Möller, J. Randrup, and S. Åberg, Phys. Rev. C **95**, 024618 (2017).
[26] M. Albertsson, B. G. Carlsson, T. Døssing, P. Möller, J. Randrup, and S. Åberg, Phys. Lett. B **803**, 135276 (2020).
[27] M. Albertsson, B. G. Carlsson, T. Døssing, P. Möller, J. Randrup, and S. Åberg, Phys. Rev. C **103**, 014609 (2021).
[28] J. Randrup and R. Vogt, Phys. Rev. C **89**, 044601 (2014).
[29] W. Hauser and H. Feshbach, Phys. Rev. **87**, 366 (1952).
[30] D. L. Bleuel *et al.*, Nucl. Instrum. Methods Phys. Res., Sect. A **624**, 691 (2010).
[31] J. Wilson (private communication).
[32] J. R. Nix and W. J. Swiatecki, Nucl. Phys. **71**, 1 (1965).
[33] H. A. Bethe, Phys. Rev. **50**, 332 (1936).
[34] F. Vivès, F.-J. Hambsch, H. Bax, and S. Oberstedt, Nucl. Phys. A **662**, 63 (2000).
[35] A. Göök, F.-J. Hambsch, and M. Vidali, Phys. Rev. C **90**, 064611 (2014).
[36] J. Blocki, Y. Boneh, J. R. Nix, J. Randrup, M. Robel, A. J. Sierk, and W. J. Swiatecki, Ann. Phys (NY). **113**, 330 (1978).
[37] C. Ishizuka, M. D. Usang, F. A. Ivanyuk, J. A. Maruhn, K. Nishio, and S. Chiba, Phys. Rev. C **96**, 064616 (2017).
[38] P. Möller, A. J. Sierk, T. Ichikawa, and H. Sagawa, At. Data Nucl. Data Tables **109-110**, 1 (2016)
[39] H. Uhrenholt, S. Åberg, A. Dobrowolski, T. Døssing, T. Ichikawa, and P. Möller, Nucl. Phys. A **913**, 127 (2013).
[40] S. Åberg, B. G. Carlsson, T. Døssing, and P. Möller, Nucl. Phys. A **941**, 97 (2015).
[41] R. Bengtsson and S. Åberg, Phys. Lett. B **172**, 277 (1986).
[42] S. Bjørnholm, A. Bohr, and B. Mottelson, in *Proceedings of the Third IAEA Symposium on the Physics and Chemistry of Fission*, Rochester, New York, 1973 (IAEA, Vienna, 1974), Vol. I, p. 367.
[43] N. Shimizu, T. Otsuka, T. Mizusaki, and M. Honma, Phys. Rev. Lett. **86**, 1171 (2001).
[44] P. Cejnar, J. Jolie, and R. F. Casten, Rev. Mod. Phys. **82**, 2155 (2010).
[45] J. Randrup and R. Vogt, Phys. Rev. C **80**, 024601 (2009).
[46] N. Dubray, H. Goutte, and J.-P. Delaroche, Phys. Rev. C **77**, 014310 (2008).
[47] P. Talou, I. Stetcu, P. Jaffke, M. E. Rising, A. E. Lovell, and T. Kawano, Comput. Phys. Commun. **269**, 108087 (2021).